Power handling and vapor shielding of pre-filled lithium divertor targets in Magnum-PSI

P. Rindt[1], T.W. Morgan[2], G.G. van Eden[2], M.A. Jaworski[3], N.J. Lopes Cardozo[1]

[1] Eindhoven University of Technology, Science and Technology of Nuclear Fusion Group, Eindhoven, The Netherlands
[2] DIFFER-Dutch Institute For Fundamental Energy Research, De Zaale 20, 5612AJ Eindhoven, The Netherlands
[3] Princeton Plasma Physics Laboratory, Princeton NJ, USA

E-mail: p.rindt@tue.nl

Abstract. To develop realistic liquid lithium divertors for future fusion reactors, this paper aims to improve understanding of its power handling capabilities. A liquid lithium divertor target prototype, designed to facilitate liquid metal experiments in tokamaks, was tested in Magnum-PSI. The target has an internal reservoir pre-filled with lithium and aims to passively re-supply the textured plasma facing surface during operation. To assess the power handling capability the target was exposed to helium plasmas with increasing power flux density in the linear plasma device Magnum-PSI. Temperature response of the lithium targets was recorded via IR camera, and compared to FEM modeling taking into account dissipation via Li in the plasma. It was found that the target works as intended and can take up to 9 ± 1 MW/m^2 for 10 seconds before the mesh layer is damaged, and could continue operating at higher power densities even after being damaged. The total lifetime of the targets was up to 100 seconds. Overall the targets are found suitable for use in tokamak experiments. Additionally, a central surface temperature evolution indicative of vapor shielding was observed on intact targets. Predicting the target temperature (and consequently the evaporation rates and thermal stresses) is considered very relevant for the design of lithium divertor targets for DEMO. The observed temperature response could indeed be replicated through modeling, which showed that a significant power fraction was dissipated by the lithium in the plasma.

Keywords: fusion, divertor, lithium, power handling, Magnum-PSI, prototype

1. Introduction

Liquid metals have been proposed as a divertor solution for future power plants [1, 2, 3, 4, 5], as they have a number of advantages over conventional solid divertors: they can be designed to be self-healing by creating a replenishing liquid metal flow [3]; extremely high power densities can in theory be tolerated in vapor shielding regimes [6, 3, 7]; the liquid itself cannot suffer damage due to the neutrons (though the substrate can); and in the case where liquid lithium (LL) is used, main plasma neutrals can be pumped to improve plasma performance, as observed in NSTX [8], FTU [9], and HT-7 [10]. Naturally though, before implementation in fusion power plants or even experimental devices, challenges remain. For example, no clear limitations to power handling have been identified yet. Experimental studies using electron beam facility SPRUT-4 have been conducted [11], and a model to predict the maximum power handling capability for liquid lithium was made [7], which can be applied to a given design but contained many free parameters. However, reliable prediction of the maximum tolerable power has not been demonstrated yet.

This paper experimentally investigates the power handling of liquid lithium divertor targets by studying a specific target design, namely the "pre-filled liquid lithium divertor target" (pre-filled LLDT) [12], shown in fig 1. This concept was originally designed for the LL experiments in the National Spherical Torus Experiment Upgrade (NSTX-U). Capillary flow through wicking channels is used to provide lithium from a reservoir to the plasma facing surface (PFS). The PFS is textured to promote further spreading of the liquid metal across the surface, essentially functioning like a capillary porous system (CPS) [13]. The wicking channels in the target also serve an important secondary function: to reduce thermal stresses by dividing the bulk material into brushes with smaller characteristic dimensions. The effectiveness of this principle is increased due to the fact that heat can still diffuse across the brushes because the channels are filled with lithium. The original design requirements for application in NSTX-U state that 5 second pulses with a local peak power density of 10 MW/m^2 must be withstood, without drying out of the PFS due to insufficient lithium supply rate and without plastic deformation of the substrate due to thermal stresses [12].

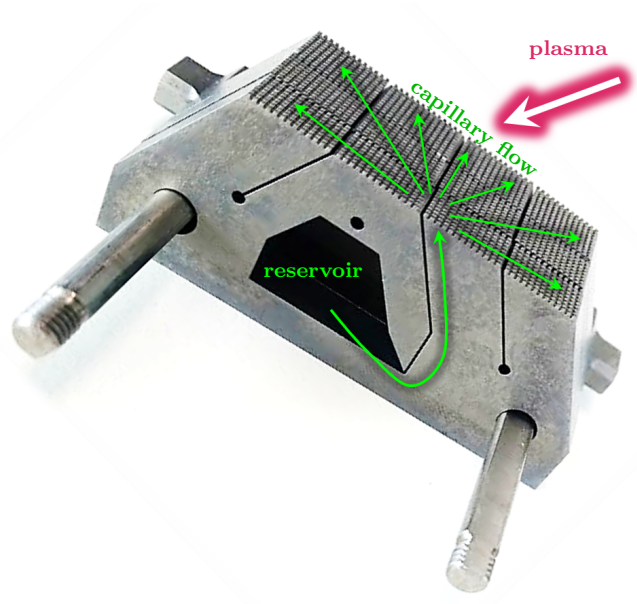

Figure 1. Titanium zirconium molybdenum alloy target used for the experiments reported in this paper, partially disassembled. The design is based on [12] and manufactured using electrode discharge machining. Lithium is transported from the reservoir via the wicks across the surface due to capillary forces. Full drawings and dimension are given in fig.2.

It is expected that vapor shielding phenomena will play an important role in power handling at high input powers. Earlier studies of this phenomenon have been performed for solid targets [14, 15], and for liquid tin [6]. It was found that when increasing the applied power density to the target a point is encountered beyond which the surface temperature is very insensitive to the applied power: a locking temperature. This was also predicted for the experiments conducted in this paper. At the locking temperature, also an oscillation of the surface temperature was observed which is explained in [16] by stating that first the tin vapor cloud creates a detachment-like plasma state which shields the target from incoming power thus allowing it to cool down. As also the vapor cloud itself cools down it enters a runaway recombination process, due to which the cloud dissipates and the surface is again heated to create a new cloud. This phenomenon is also expected to be valid here.

The approach of this work is to increase the loading of the target until it is damaged. The experimental results will then be compared to the model from [7]. In this model the power coming from upstream in the plasma is balanced against the thermally conducted power Q_{cond} and the power dissipated by the lithium lost from the surface, which are both temperature dependent terms. When the dissipation via the lithium vapor becomes dominant over the conductive dissipation, a locking temperature is predicted by this model, as observed for tin.

$$Q_{plasma} = Q_{cond} + Q_{loss} \tag{1}$$

$$Q_{loss} = \Gamma_{loss,net} \cdot (\epsilon_{cool} + \epsilon_{rem}) \tag{2}$$

Each particle then dissipates an amount of energy required to remove it from the surface (ϵ_{rem}), plus energy radiated in the plasma and taken up by the increase of potential and kinetic energy of the evaporated particle (ϵ_{cool}). In case the contribution from radiation is small compared to the total, ϵ_{cool} is only dissipated when particles do not return to the PFS, and deposit their potential and kinetic energy elsewhere. According to [17], this is indeed the case for the plasma conditions in Magnum-PSI, and hence ϵ_{cool} is only dissipated for the net loss flux from the PFS. This flux, $\Gamma_{loss,net}$, may be approximated as an evaporative loss Γ_{vap} corrected for the redeposition R, in which case ϵ_{rem} equals the latent heat of vaporization. When the net loss flux exceeds the available supply, the target dries out and the maximum tolerable power is found.

The lithium supply consists of a flow driven by capillary forces. As the porous texturing on the PFS has much smaller characteristic dimensions than the reservoir, the flow is driven towards the surface (until the texture is saturated). In [12] a supply rate of up to $2 \cdot 10^{25}$ $\mathrm{m^{-2}s^{-1}}$ is predicted for the original design, using an analytical model based on the Darcy equation. A similar supply rate is expected for the prototypes used here, as the characteristic dimensions are similar.

The experimental results in this paper are obtained using linear plasma device Magnum-PSI [18, 19] to apply heat loads up to 9 $\mathrm{MW/m^2}$, while simultaneously monitoring surface temperature and lithium light emission. The relevant components of Magnum-PSI, and the exact target design are detailed in section 2. The obtained data is presented in section 3. Interpretation of the experimental data, including comparison to predictions from [7], is then given in section 4. The paper concludes with the assessment of the performance of the design and design recommendations which will allow implementation in a tokamak for experimental purposes.

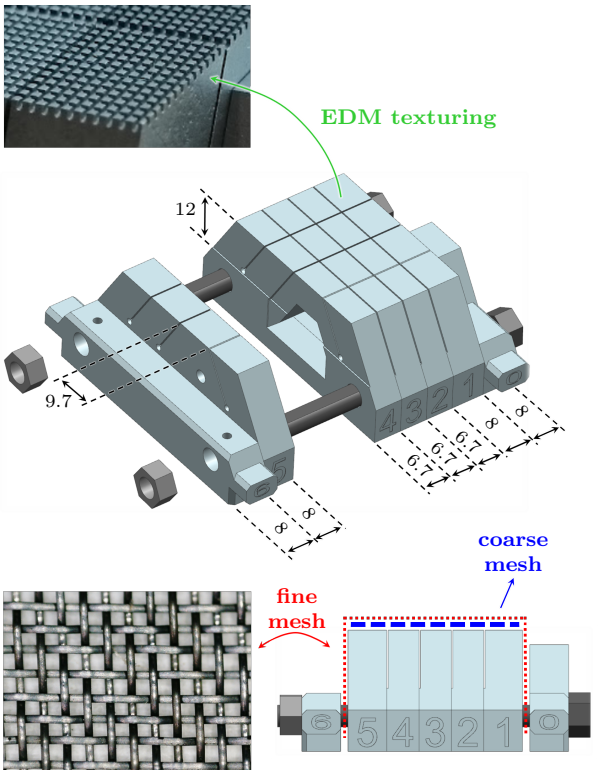

Figure 2. Detailed overview of the prototype design, consisting of 7 TZM layers held together with steel bolts. Target height is 25 mm in total. The wicking channels are 300 μm wide. Three target types are used: with the EDM texturing (top) or the mesh layers (bottom) applied, or with the EDM texturing and the fine mesh combined. The EDM texturing has cuts of 300 micron wide, 450 micron deep, and 450 micron apart measured from edge to edge. The fine mesh has 50 micron thick wires with square pores of 100 micron wide. The coarse mesh has 160 micron thick wires and 260 micron wide pores.

2. Experimental method

2.1. Target design

The target design and dimensions are shown in figure 2. The design is based on the original design for NSTX-U [12], but adapted for Magnum-PSI. The aim is to use capillary forces to passively supply the PFS with lithium from the reservoir via the wicking channels. The targets are composed of 7 layers of titanium zirconium molybdenum alloy (TZM) which were cut from the raw material using wire electrode discharge machining (EDM). The wicking channels are 300 micron wide, and together with the reservoir have a volume of 4.7 $\mathrm{cm^3}$, sufficient to hold 2.4 grams of lithium. Note that as the Magnum-PSI plasma beam is oriented horizontally, the targets are mounted vertically. The wicking channels connect in this configuration to the bottom of the reservoir so that the reservoir can be fully depleted. Two stainless steel bolts hold the layers together.

Three variants of the target were used in the experiment, each with a different surface texturing. The first type is the so-called *EDM-type*, where the texturing is cut into the surface using EDM. The cuts are 300 micron wide, 450 micron deep, and 450 micron apart measured from edge to edge (fig. 2). The second type, named *combi-type*, uses the same EDM texturing but has a mesh layer applied on top of this. This layer is fixed by clamping it between the outer two layers of the target. Unfortunately, this method does not allow for tightening the mesh around the surface, which results in the presence of some play between the mesh layer and the surface. The distance between the mesh and the surface is estimated to be up to 1 or 2 mm. The mesh is supplied by Unique Wire Weaving Co., Inc. and has 165 wires per inch with a diameter of 0.002

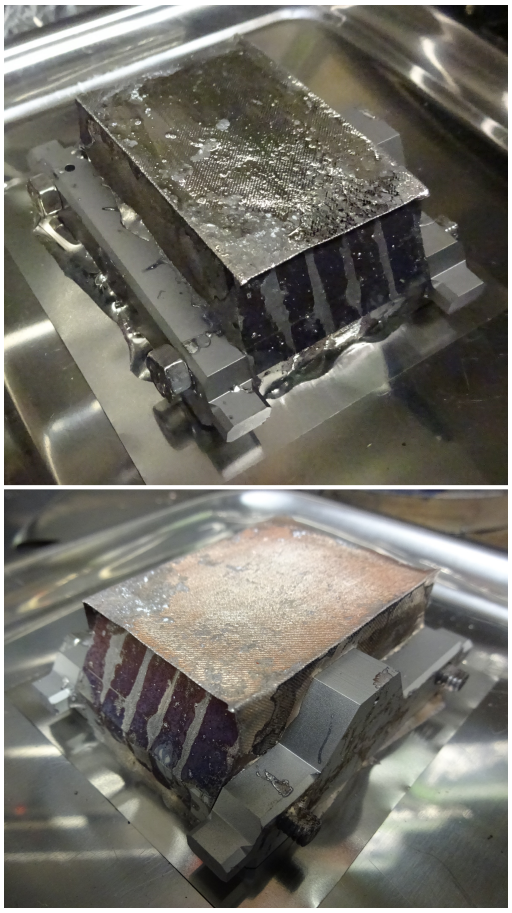

Figure 3. Filled targets inside the glovebox with still liquid lithium (top) and solidified lithium (bottom). Minor discoloration still occurs despite the argon atmosphere. The individual plates are first wetted with scraping tools, then assembled while hot after which the mesh is placed on and clamped. Then the targets placed on a steel foil to cool.

inch in a twill weave. This translates to a mesh with 50 micron thick wires with square pores of 100 micron wide in between. The third and final texturing uses only mesh layers and no EDM texturing and is called *mesh-type*. The aforementioned mesh layer is used as a top layer, but a coarser mesh is placed beneath it with 160 micron thick wires and 260 micron wide pores. Only the fine mesh layer on top is clamped.

After manufacturing the targets were filled with lithium. To this end, first oxides were removed from the plates using dry sand blasting. Subsequently the targets were cleaned in a sonic acetone bath, and then rinsed with ethanol. The lithium filling was performed in an argon atmosphere glove-box with oxygen and moisture levels below 5 ppm. To ensure wetting, first each of the plates is wetted individually in a lithium bath, which was heated by a hot plate. Stainless steel mechanical scraping tools were used to ensure wetting also in the reservoir and in all wicks. The EDM textured PFS could not be wetted in a straightforward manner. Partial wetting was achieved by placing the plates upside down in a 400 ^{o}C lithium bath for up to 10 minutes. The Li did wet the PFS of the EDM-type target sufficiently when exposed to the plasma beam. The mesh layers could however be fully wetted and are placed on the surface during assembly. While the target was still hot, the bolts were inserted and tightened, thus clamping the mesh layers. The target was then placed on a steel foil to cool down. When liquid, the lithium had a mirror-like appearance, but some discoloration occurred already after cooling (fig. 3). This indicates that despite the use of the glovebox, some chemical interaction still occurred.

One target of each type is mounted on the target holder in Magnum-PSI. This target holder can hold five targets simultaneously, and it can be rotated so that each of the targets can be individually exposed to the plasma, without breaking vacuum. Hence, the lithium targets are only oxidized once during mounting. An image of the target holder can be found in [22]. Apart from the three lithium targets, two other targets filled the available places on the target holder. A tungsten dummy target to test exposure sequences and diagnostic alignment (not discussed further), and one so-called *blank* target. The blank is identical to the EDM-type targets, except it was not filled with lithium and no surface texturing was applied. All targets are clamped to the target holder, which consists of a 4

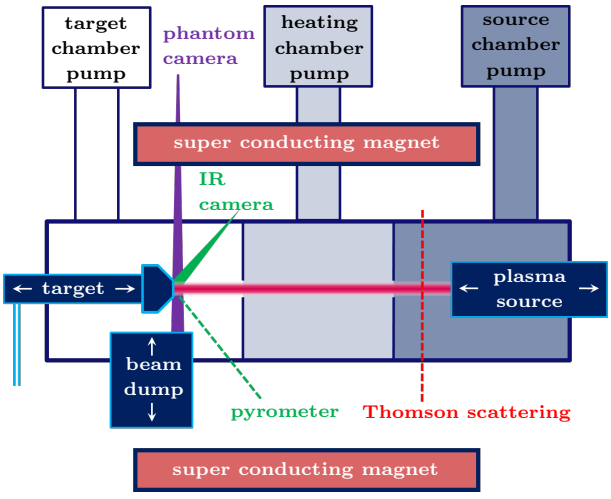

Figure 4. Overview of Magnum-PSI [19, 20, 21] and the subsystems relevant to this paper. On the target holder 3 lithium targets and 1 blank target are mounted. They are exposed by the plasma from a cascaded source. The three different chambers are differentially pumped to achieve better plasma parameters. Used diagnostics are the pyrometer, IR camera, and Phantom camera filtered at 670.8 nm. Thomson scattering was only available at the plasma source location. To move the target into exposure position requires that the beam dump is moved down (as depicted). The complete transition takes around 7 seconds. All diagnostics only have a view of the target in exposure position.

Shot no.	target type	B-field [T]	gas flow [slm]	I_s [A]	estimated peak power density [MW/m^2]
36	combi	1.2	12	120	9±1
42	mesh	0.6	12	120	(cleaning)
43	combi	0.6	12	120	(cleaning)
44	combi	0.6	12	120	(cleaning)
46	blank	1.2	12	120	9±1
48	mesh	1.2	14	120	8±1
49	combi	1.2	14	120	8±1
50	blank	1.2	14	120	8±1
52	mesh	1.2	12	120	9±1
53	combi	1.2	12	120	9±1
54	combi	1.2	10	120	10±1 *
55	mesh	1.2	10	120	10±1 *
74	combi no.2	1.2	12	120	9±1
77	combi no.2	1.2	14	120	8±1

Table 1. Overview of the experimental plan on Magnum-PSI. Discharges are arranged in chronological order. Intermediate non-relevant discharges have been omitted. Discharge 77 is performed some time after the other discharges. The machine settings (B-field strength and source gas flow and source current I_s) are given along with the estimated peak power density resulting on the target. Helium is used in all discharges. *The peak power density for shot 54 and 55 could not be determined via matching of the FEM modeling to the observed temperature (see sec. 2.4). Rather, it is extrapolated from the observed correlation between source gas flow and peak power density for earlier discharges.

mm thick copper surface which is water cooled on the back. To enhance thermal contact a Grafoil flexible graphite layer was clamped between the target and the holder. The targets without lithium are mounted first, so that after mounting the lithium targets, the chamber can immediately be pumped down to around 0.1 Pa. Despite these steps, reactions of the targets with atmosphere could not be completely prevented, as indicated by the dull grey/blue-ish discoloration observed.

2.2. Magnum-PSI

A schematic overview of Magnum-PSI is shown in figure 4, including only components relevant to this work. The working and usage of these components is described here. Further details can be found in [19, 20, 21].

The plasma is created by a cascaded arc source inside a magnetic field, resulting in a beam that is impacting on the target. Densities and temperatures around 10^{20} m^{-3} and 1-5 eV can be typically achieved [19]. A helium plasma was used to avoid any chemical interaction with the lithium on the PFS as would occur for hydrogen [23, 24]. The main concern is that solid lithium hydride formed on the surface could block the capillary flow. Low power helium discharges were also used to clean oxides that are created during target mounting from the lithium layer (sec. 3). Of course, the interaction between helium and lithium in the plasma is different than it would be between hydrogen and lithium. Obtained results regarding the effectiveness of vapor shielding, can therefore not be directly translated to performance in tokamak experiments.

The targets were held at floating potential in all cases. An overview of the discharges presented in this paper is shown in table 1. Note that the discharges are shown in chronological order. Shot number 74 and 77 have been performed on a second combi-type target some time after the other discharges, denoted by the additional horizontal lines. Intermediate shots that are not considered in this work have been left out for convenience, but the full experimental log can be found in the replication package [25]. In cases where the full history of the targets is relevant, this is noted in the text (e.g. because damage occurred earlier).

The plasma exposures are composed of four phases which are necessary due to the fact that Magnum-PSI makes use of 1) a beam dump, and 2) a standby plasma. Regarding the first phase: The beam dump is located in the target exposure position. When it is moved down, the target is immediately exposed and is then translated forward $\sim$ 60 cm to exposure position. The standby plasma was a low power helium plasma. When the beam dump and target started moving, the standby plasma was changed simultaneously into the desired plasma (as specified in table 1). As this is not standard

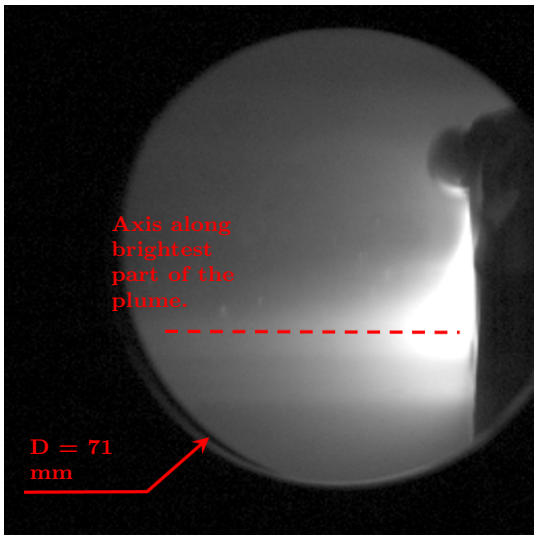

Figure 5. View of the Phantom camera perpendicular to the target (right), ∼12 s into discharge 52. A 670.8 nm filter is applied to capture the light emitted by the lithium inside the plasma beam (which is coming from the left). The red line marks the axis along the brightest part of the plume, against which the intensity is plotted in fig. 13. Length scales are inferred from the size of the window.

operation, manual timing was required. Consequently, the desired plasma conditions were reached roughly 1 or 2 seconds after beam dump and target motion was complete, roughly 7 to 8 seconds after the start of the entire procedure.

Phase 2 then consisted of the exposure of the target to the desired conditions for the desired amount of time. This phase is from hereon referred to as the main plasma. A main plasma of 10 seconds on the lithium targets was chosen to approach steady state conditions, while preserving sufficiently lithium for further exposures. Discharge number 46 on the blank target had only 5 seconds of main plasma to prevent damage to the target at high power. Discharge number 77 was continued longer to find out after what time the lithium would be depleted. Phase 3 and 4 consisted of changing the plasma back to the standby settings, and subsequently moving the target and beam dump back.

2.3. Diagnostics

The key parameters to measure were the target temperature and deposited power. Both rely on the pyrometer and infrared camera, which are a FAR SpectroPyrometer model FMPI s/n 7343-1114 and FLIR SC7500MB respectively. The IR camera measures in the 2 to 5 μm range at low temperatures or 3.97 to 4.01 μm range at high temperatures, depending on the filter chosen. To determine the transmittance of the IR optical system, the emissivity of the blank target was taken from literature, and the transmittance was determined via comparison against the temperature measurement by the pyrometer. Considering discharge number 50, and taking a constant emissivity of 0.15, estimated from [26, 27, 28], this resulted in a transmittance of 22%. Applying these values to six comparable exposures on the blank targets resulted in a deviation of maximum ± 50 ^{o}C from the pyrometer measurements. This implies that the transmittance did not strongly vary during the experimental period.

Pyrometer measurements on the lithium targets were not possible because no good signal quality could be obtained. Therefore only the IR camera was used, and the transmittance determined with the blank target was assumed to be valid. The emissivity of Li was taken to be 0.1 in the measured temperature range [27]. Changing the emissivity assumed for the lithium or the blank target by 20%, results in a $\pm 65^o$C change in the measured Li temperature. The assumption for the transmittance did not hold for shot 77, as it was performed days later, during which period the transmittance was suspected to have changed. Usable pyrometer measurements on the blank target around the time of shot 77 are not available, thus making it impossible to accurately determine the temperature here.

Finally, light emitted by Li-I in the plasma was observed via a Vision Research Phantom v12.1 camera fitted with a 670.8 nm filter. This camera has a perpendicular view of the plasma beam directly in front of the target. As shown in figure 5, the view extends approximately 5.5 cm in front of the target into the plasma. Due to limited dynamic range the image was often saturated in the region until 0.5 cm from the target. Images were acquired with a frequency of either 400 or 4000 Hz depending on the plasma exposure.

2.4. FEM-modeling

To determine the deposited power on the blank targets a finite element method (FEM) model was constructed in Comsol 5.1. The power flux density applied in the experiment is found by tuning the power flux density in the model, so that the modeled temperature corresponds to the temperature observed experimentally.

The geometry shown in figure 6 was used in the model. Computational time was reduced by applying a symmetry boundary condition. The Grafoil between the target and the copper was modeled as a thin boundary layer with a thermal resistance of $1 \cdot 10^{-4}$ Km^2/W. The backside of the copper was fixed at

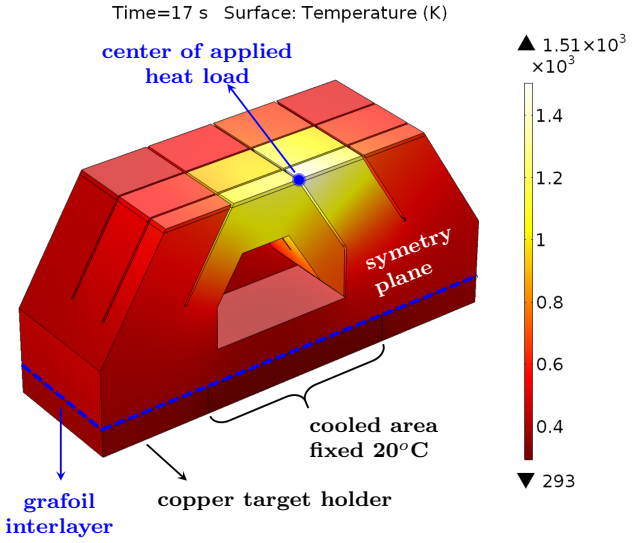

Figure 6. Setup of the FEM model of the blank target (without lithium), and temperature result. A heat load with Gaussian distribution is applied in the center of the top surface, FWHM = 19 mm. A symmetry plane is used to reduce computation time. The Grafoil interlayer is mimicked by using a thin layer with a thermal resistance of 10^{-4} Km^2/W, based on a thickness of 0.3 mm and a conductivity of 3 W/mK [29]. The copper from the target holder is also included in the model, where the central area with radius 14 mm has a fixed bottom temperature of 20 ^{o}C.

293.15 K. A heat flux was applied in the center of the PFC with a Gaussian profile (FWHM of 19 mm, as inferred from Thomson scattering). All other surfaces were insulated and radiation losses were found to be negligible and were therefore omitted in the final simulations. The exact material properties are given in the replication package.

The time dependence of the heat load is illustrated in figure 7. Both the increase in power due to target motion and due to the plasma transition were modeled as a linear ramp over a factor 0.5 in 7 seconds. The insertion of the beam dump at the end of the discharge is modeled as a sharp cut-off. In the simulation, the change in applied power is taken as the linear combination of both effects. The only remaining free variable in the model is the applied peak power density during the main plasma, which was tuned to match the IR camera measurement. It should be noted that the simulation outcome is not influenced by the exact shape of the trajectory, beyond the indicated uncertainty of the applied power density in table 1. Hence, this estimate of the heat load time dependence is deemed sufficiently accurate.

Both the experimental result and modeling for discharge 50 and 46 are shown in figure 8. The

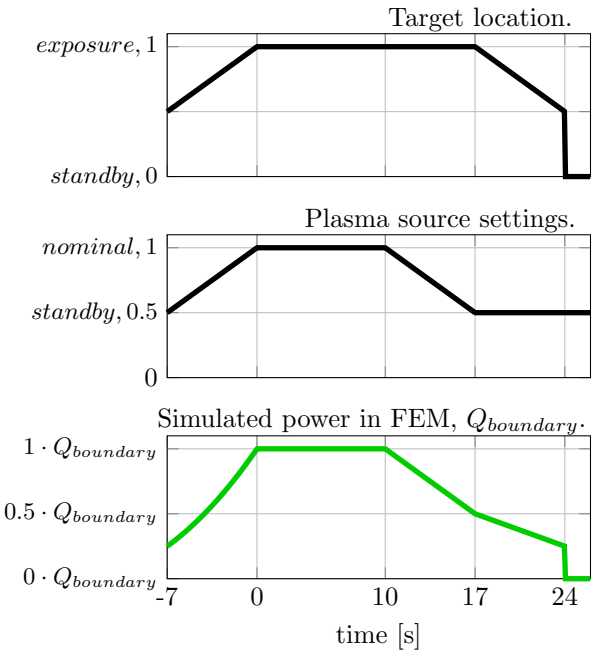

Figure 7. $Q_{boundary}$ in the FEM model is taken as the linear combination of functions in the top two panes. The target motion increases the relative power from 0 to 1, as in the stand-by position the target is completely shielded by the beam-dump. The plasma source settings increase the relative power density from 0.5 to 1, as also the stand-by plasma deposits power. In reality the change is plasma settings is triggered manually after the target motion is initiated, creating a slight delay. The target comes into view of the IR camera at 0 seconds.

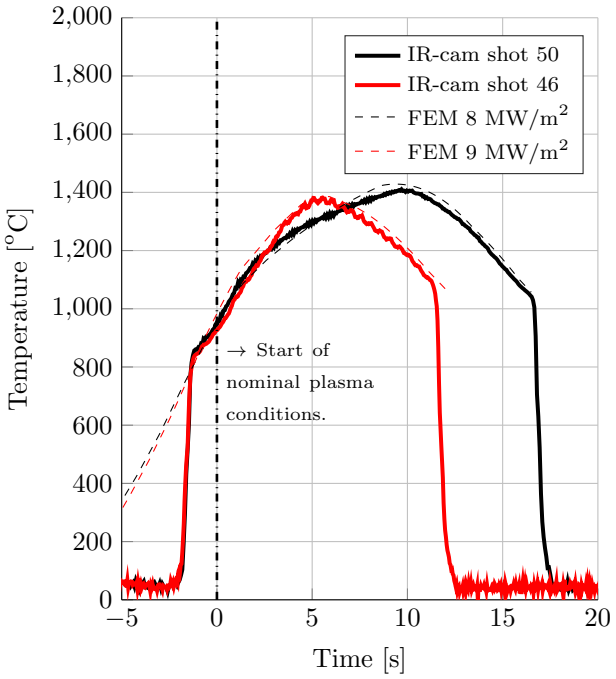

Figure 8. FEM model output matched to IR-camera recordings for shot 50 and 46. The peak power density during the steady state period of the discharges is found to be 8 and 9 MW/m^2 respectively. The error is estimated at ±1 MW/m^2, taking into account the uncertainty in the IR measurement and the assumptions underlying in the FEM model. The steep increase and decrease at the beginning and end of the discharges are merely when the target comes into view of the IR camera. Note that the FEM results have been slightly shifted along the time axis to correct for the errors in the manual timing of the experiment. Hence the two FEM curves are not synchronized.

peak heat flux density was found to be 8±1 and 9±1 MW/m^2 respectively (given the uncertainty in the temperature measurement). The increase in flux density between these shots was achieved by lowering the source gas flow from 14 slm to 12 slm. These discharges were used to infer the applied power density for the lithium exposures except for the cleaning discharges and discharge 55, as for these cases no comparable discharges on the blank target are available. For discharge 55 the peak heat flux density was assumed to be linearly increased to 10±1 MW/m^2, because the source gas flow was also linearly decreased to 10 slm. Nevertheless this remains an assumption.

3. Results

In this section, temperature measurements and measurements of 670.8 nm light are presented. At the beginning of the shot series, all targets were exposed to low intensity plasmas to remove macroscopic oxides created during mounting, and to make sure capillary flow was not impeded by these oxides. See for example exposure 43 in table 1. As soon as the targets were

heated to just above the melting point the dull gray color changed into a shiny silver color, indicating that the oxide removal was successful, see figure 9. Results from the EDM-type targets are not presented as this target dried out prematurely.

Exposure of the EDM-type target to low intensity plasmas resulted in a clean shiny surface, comparable to figure 9. However, after exposure to plasmas at 1.2 Tesla the PFS appeared to be dry, as observed from IR footage, absolute temperature levels, and visual inspection. The target PFS could not be re-wetted by exposure to the low intensity plasma, and neither the IR footage nor the Phantom camera recordings indicate droplet ejection or other macroscopic loss of lithium from this target. Hence the drying could have been caused by a depleted lithium reservoir due to insufficient filling, or failure to resupply the PFS from the reservoir.

During all plasma exposures, the Li influenced the surface temperature distribution. The temperature distribution had point symmetry as shown in figure 10, whereas without lithium the individual brushes could be made out clearly.

The presence of Li also suppressed the surface temperature, which could be observed at power densities of $\sim$9 MW/m^2 in shot 48, 49, 52 and 55, see figure 11. Time traces of the target temperature at the beam center are shown for exposures of the lithium targets, and for the blank target. The latter reached significantly higher temperatures. Not all temperature evolutions on the lithium targets were similar, but also there was a difference in the targets. The mesh-type

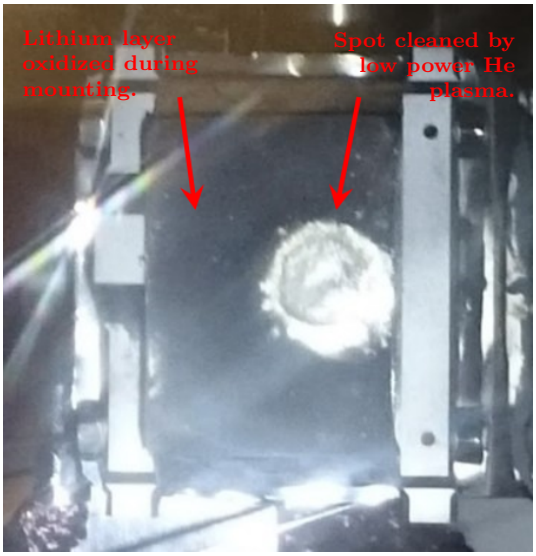

Figure 9. Oxidized Li target photographed trough the vacuum chamber window. Exposure to a low power He plasma liquefied the target locally and returned the surface to a silvery shiny state.

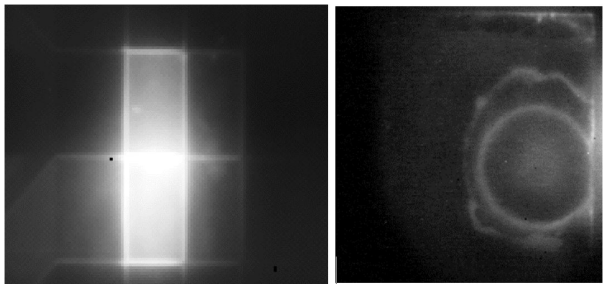

Figure 10. Temperature distribution across the surface without lithium (left) and with lithium in shot 43 (right). Without lithium the heat cannot spread across different brushes. The empty wicks act like black-body radiators and light up. On the contrary, when lithium is present, heat is distributed equally in all directions and an almost perfectly circular melting front is observed.

target which was used for shot 48 and 52, was fully intact. A combi-type target with a hole in the mesh was used in shot 49. The hole was created in previous discharges, exposing the EDM texturing underneath, see figure 12. This difference played a significant role, as further discussed in section 4. The temperature evolution for shot 74 is not shown in this figure, as not calibration was possible for the IR camera. The mesh on this target was still intact in this shot, and the temperature evolution was similar to that in shot 48 and 52.

The temperature evolution when the mesh of the mesh-type target was eventually destroyed in shot 55 is also shown in figure 11. The underlying mesh layer was not damaged. The hole in the mesh was observed through a view-port immediately after the discharge. Directly after the temperature spike where the mesh is suspected to have melted, the temperature returns to reduced levels compared to those on the blank. The maximum peak power density any target has withstood without damage is 9 ± 1 MW/m^2, discharge 52.

Temperature oscillations were observed during discharge 48 and with more constant frequency in shot 52. The amplitude was similar in both cases, however, the oscillation time and shape varied widely. The first four oscillations in shot 52, during the steady state plasma, had a period of $\sim$1 second. In discharge 48 though the period times were between $\sim$0.5 and $\sim$1.5 seconds. The steady temperature plateau that preceded the oscillations, from 0 s until 4 s, was very similar in both discharges. Oscillations in the light observed by the Phantom camera were not observed. Though, the image was saturated within 10 mm from the target. Finally, faster oscillations with a frequency of 20 Hz were also present in the camera signal. These however also occur on the reference shots on the dummy target, and were due to the vibration of the camera holder and optics, which were in turn caused by the vacuum pumps of Magnum-PSI.

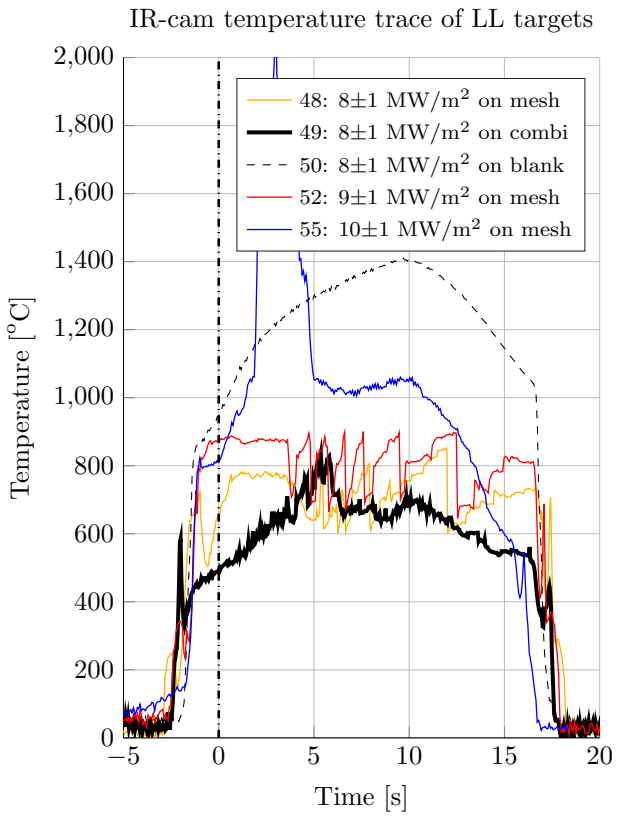

Figure 11. Observed temperature evolution of LL targets. A combi-type sample (bold, black) with a hole in the mesh layer is exposed in shot 49. The mesh-type targets have an intact mesh layer in shot 48 and 52 until it is destroyed in shot 55 marked by the large temperature spike. Notably after this spike the surface reaches a steady state again before the shot ends at 10s, at a temperature well below that of the blank targets in fig. 8.

The Phantom camera has been used for two purposes. First of all, the axial intensity profile is plotted for a variety of discharges, see figure 13. This intensity profile was taken where the plume is found to extend furthest into the plasma for every discharge (fig. 5), and averaged over the duration of the discharge. On first view, two parameters were of clear influence on the intensity: First, the magnetic field, which is known from literature to influence the thickness of the shielding layer by limiting transport of ions perpendicular to the field [30, 31]; And second, the target type, which results in different intensities even for constant magnetic fields. Also indicated in the figure is whether the mesh layer has a hole in it or is intact.

Secondly, the intensity in front of the target during exposure 77 was used to determine after what time lithium was no longer evaporating from the surface. In figure 14 it can be seen that from the start of the discharge first the intensity increased almost by an order of magnitude before falling suddenly at ∼60 seconds, after which the exposure was terminated manually at ∼80 seconds. This particular target was exposed to already four 10 s high power discharges before shot 77.

4. Discussion

4.1. Prototype performance

The prototypes have demonstrated that the pre-filled target concept can work successfully. All wicking channels have been wetted during pre-filling in the glovebox, and heat was conducted across them. This is apparent from the changed surface temperature profile, figure 10. The cleaning procedure, required to remove the oxides obstructing the capillary flow, is also found to be successful.

The total lifetime of the component can be up to 100 seconds, as demonstrated by the second combi-type target which lasted $4 \cdot 10 + 60$ seconds. This can be translated as at least 20 discharges of 5 seconds in NSTX-U. But most likely the lifetime would be much longer. This is firstly because the ramp-up and down phases during the experiments in Magnum-PSI are not considered. Secondly, due to the length of discharge 77, the outer areas of the target have heated up more than they would in a 5 second discharge. These areas were not exposed to the plasma and there was no redeposition, so large amounts of lithium were likely evaporated from here. Moreover, the electron and ion temperature at the target in NSTX-U will likely be higher than in Magnum-PSI. This will increase the

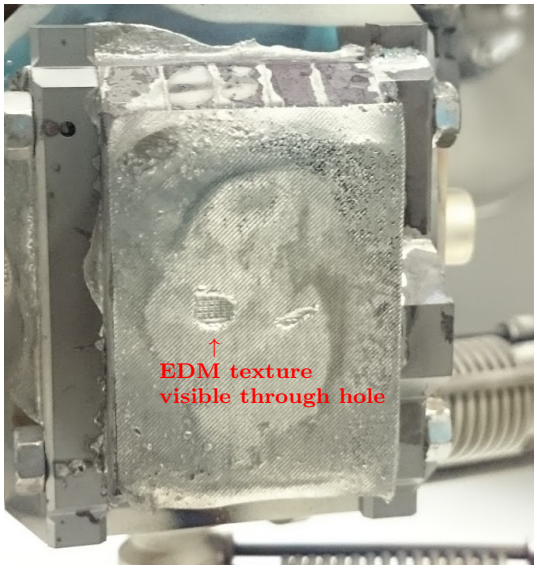

Figure 12. Post-mortem picture of the combi-type target no. 2. The mesh has been melted to create a hole in both exposure positions. Through the large hole the underlying EDM texturing can be seen.

amount of energy dissipated per Li particle (ϵ_{cool}) [17]. In turn this will increase the effectiveness of the shielding, which will ultimately reduce the surface temperature and evaporation rate, thus increasing the expected lifetime.

Two limiting factors to the lifetime in NSTX-U compared to the lifetime in Magnum-PSI must also be considered. First, as mentioned in section 2.2, helium is used instead of hydrogen. In hydrogen ϵ_{cool} could be different than in helium, though likely the aforementioned effect of increased electron and ion temperature will be dominant, and ϵ_{cool} will still be increased in NSTX-U compared to Magnum-PSI. Second, strong evaporation during millisecond transients (e.g. ELMs), could be more significant than the losses in steady state. Though, resilience against transient events by Li CPS systems has been demonstrated in [32], it is recommended to investigate the effect of transient loading on the lifetime for the specific design used here.

A peak power density of 9 ± 1 MW/m^2 can be withstood for 10 seconds without damage. Beyond this point a hole in the top mesh layer was always created. This is just below the requirement originally formulated for NSTX-U. When damaged though, the targets could still be used, as evident from discharge 49, 55 and 77.

It is suspected that the mesh was damaged due to poor contact with the substrate. Figure 11 shows that with an intact mesh layer (shot 48 and 52) the temperature at the start of the discharge (0 seconds) was twice as high, compared to when there was a hole in the mesh layer and the plasma impacted the bulk directly (shot 49). Shot 74 was performed on a combi-type target with an intact mesh. The temperature response for this target is not displayed because for both shot 74 and 77 calibration of the IR camera was not possible. However, the shape of the temperature evolution for shot 74 resembles the shape observed for shot 48 and 52 closely. Indicating that indeed the hole in the mesh layer was responsible for the change in temperature evolution, and not necessarily the target type.

The quick temperature rise on intact mesh layers was likely also responsible for the increased intensity of the Li I light for the mesh-type targets, measured by the Phantom camera in figure 13. Though, another possible explanation, which cannot be excluded, is the presence of the second mesh layer in the mesh-type targets. Comparing shot 55 to shot 48 and 52, does indicate the difference between an intact and a damaged mesh layer, but it should be noted that the damage was created during shot 55 itself. Also, this discharge was performed at a higher beam power than shots 48 and 52.

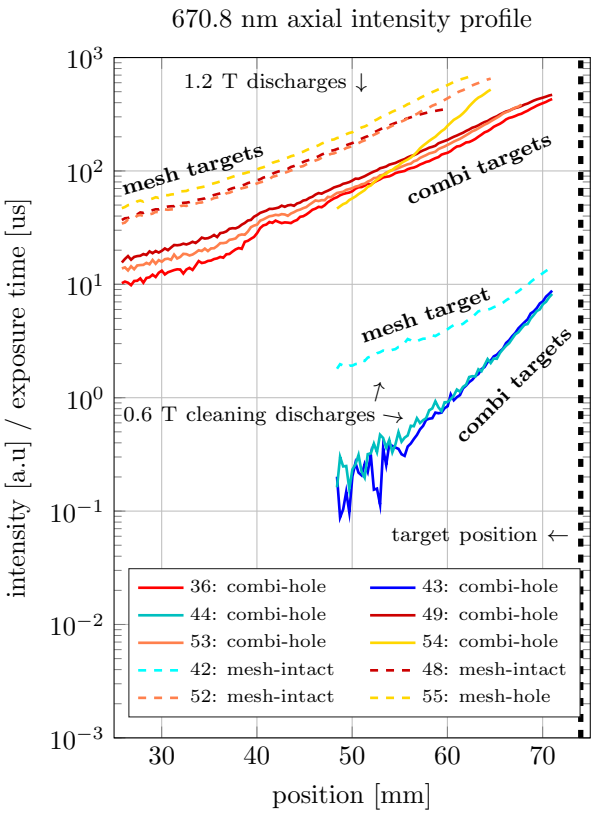

Figure 13. Axial intensity profile of 670.8 nm light observed by the Phantom camera, averaged over the discharge. The profile is evaluated on the axis where the plume is highest, as indicated in fig. 5. The target position is on the right. Clearly, a strong dependence on target type as well as magnetic field is present.

Given that the mesh was only clamped at the sides and not fixated to the the PFS, it is very likely that local heating of the mesh has resulted in bulging. This could have led to a poor thermal contact and reduced Li supply, which in turn led to overheating and melting. This hypothesis is supported by the temperature modeling in sec. 4.3, and implies that improvement of the surface texturing could allow use under higher heat loads.

4.2. Vapor shielding

Vapor shielding is found to be significant during discharges 48 and 52. Signatures were observed that were also found on tin [6, 16]: both reduced as well as oscillating surface temperatures.

In the beginning of the discharges, surface temperatures in shot 48 and 52 specifically appeared to rise at least as fast as on the blank target, but then suddenly reached a temperature plateau. As known from earlier studies on solid targets [14, 15], locking at a specific temperature is caused by the strong dependence of the vapor pressure on temperature.

Because the vapor dissipates power in the plasma, less power needs to be conducted and the surface temperature is reduced. A more precise estimate of the fraction of the incoming power that was shielded is obtained through the modeling in sec. 4.3.

Oscillating behavior was also observed on the IR camera, most clearly for shot 52. The frequency and amplitude of this oscillation are comparable to the oscillations observed on tin [16]. There, two oscillations were observed at a frequency of ∼250 ms and ∼2.5 seconds, with an amplitude around ∼200 and ∼300-400 degrees respectively. This is similar to the frequency and amplitude observed here. The shape of the oscillation though is not exactly the same. In [16] three phases are described where first the temperature gradually increases, then a steady state is reached, and finally a steep drop occurs. In this case there is also a steep drop followed by a recovery phase, but the recovery phase consists instead of first a sharp rise, and then a gradual increase until the drop.

Furthermore, the oscillations are not recognizable in the Li I light observed by the Phantom camera, whereas for tin this was certainly the case [16]. A possible explanation is that due to the large PFS, the Li concentration in the plasma was dominated by the surface region at the edge or outside the plasma beam. Namely, as for tin, it is expected that Li from the beam center is rapidly ionized before it can reach the plasma edge. Meanwhile, Li evaporated from the target edge could move towards the beam and be excited at the edge before ionization (these particles should generally be described using kinetic theory rather than fluid theory [33]). Thus, the light emitted by neutral Li, would be dominated from lithium evaporated from the target edge.

Whether the same mechanism as proposed in [16] was indeed responsible for the temperature oscillations observed here cannot be determined, as also the mesh can play a role which cannot be excluded. The mesh, or the liquid underneath could have moved, and may in that way have also caused an oscillation. Though, also in [16] mesh layers were used.

4.3. Temperature modeling

Modeling was used to predict the target temperature response, as well as the lifetime before lithium is depleted. A finite element method model implemented in Comsol 5.1 was used to simulate the conductive behavior, while the vapor shielded power was approximated using the analytical model from [7], presented in the introduction. Specifically, vapor shielding was accounted for by setting boundary heat flux density as follows:

$$q_{boundary} = q_{plasma}(r) - q_{vap}(T) \tag{3}$$

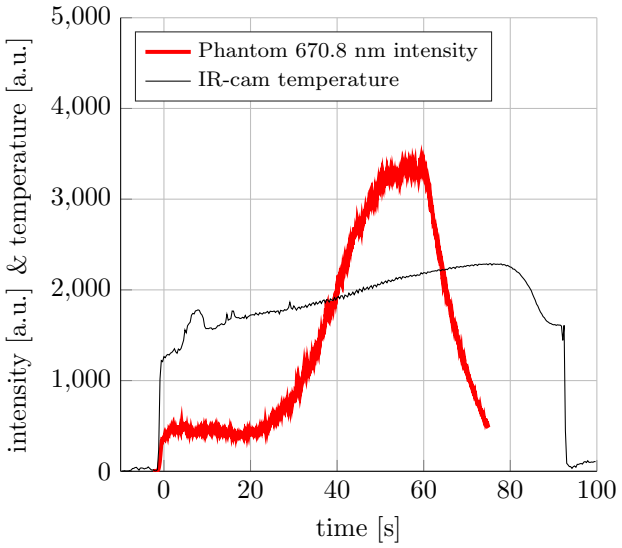

Figure 14. Time evolution of the 670.8 nm light emission compared to the surface temperature during shot 77. The 670.8 nm light intensity starts out constant but then rapidly increases until a rapid decrease at 60 s. The temperature shows a slow increase until ∼80 s when the shot is manually terminated. The IR camera could not be calibrated against the pyrometer due to lack of usable data near the time of the shot.

Here the $q_{boundary}(r,T)$ is the heat flux density applied to the PFS in the model, representative of Q_{cond} in eq. 1. q_{plasma} is the power density supplied by the beam, as determined using the blank target. q_{vap} is the power dissipated by the lithium vapor, and is described in equation 4.

$$q_{vap} = \gamma_{vap}(T) \cdot (1 - R) \cdot (\epsilon_{cool} + \epsilon_{vap}) \tag{4}$$

In this equation $\gamma_{vap}(T)$ is the local evaporation flux density calculated according to the Langmuir evaporation law. ϵ_{vap} and ϵ_{cool} are taken as 1.6 eV and 5 eV respectively. This is derived from [17], given the typical plasma conditions in Magnum-PSI. Comsol solves the FEM model, with boundary condition from eq. 3 and 4, for the temperature T.

Two different geometries have been used. To model the case with a damaged mesh layer (shot 49) thermal conduction across the wicks was assumed as good as for bulk tungsten, and thus the wicking channels were completely neglected. The reservoir was assumed empty. Lithium on the PFS was neglected completely as the layer thickness was estimated on the order of 30 micron only. This was derived from figure 12, where the EDM texturing can be clearly made out despite being wetted, indicating that the lithium thickness was well below the characteristic size of the texturing (300 micron). To model the case where the mesh was intact, the suspected loss of contact with the bulk (sec. 4.1) is mimicked by including an artificial bubble. The top 0.5 mm of the target was modeled

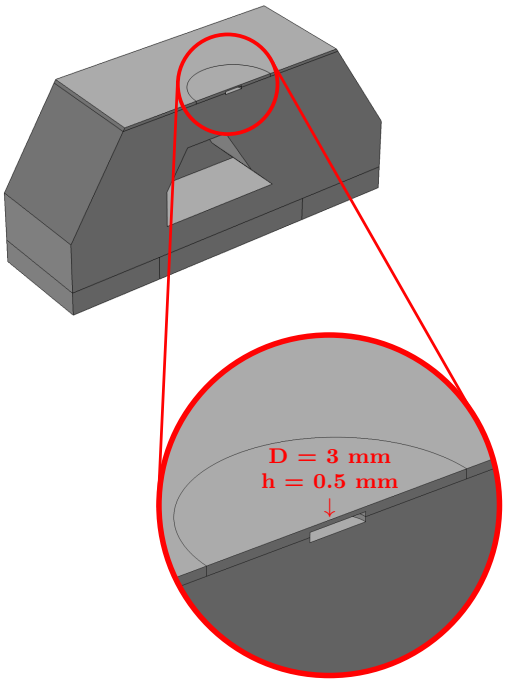

Figure 15. Adapted FEM geometry to simulate wetted targets. To model shot 49, all wicks and the surface Li layer are assumed negligible. The reservoir is left empty. To model shot 52 the top 0.5 mm is modeled as lithium, and an artificial bubble is added 0.25 mm below the surface. The bubble has cylindrical shape with D = 3 mm and h = 0.5 mm.

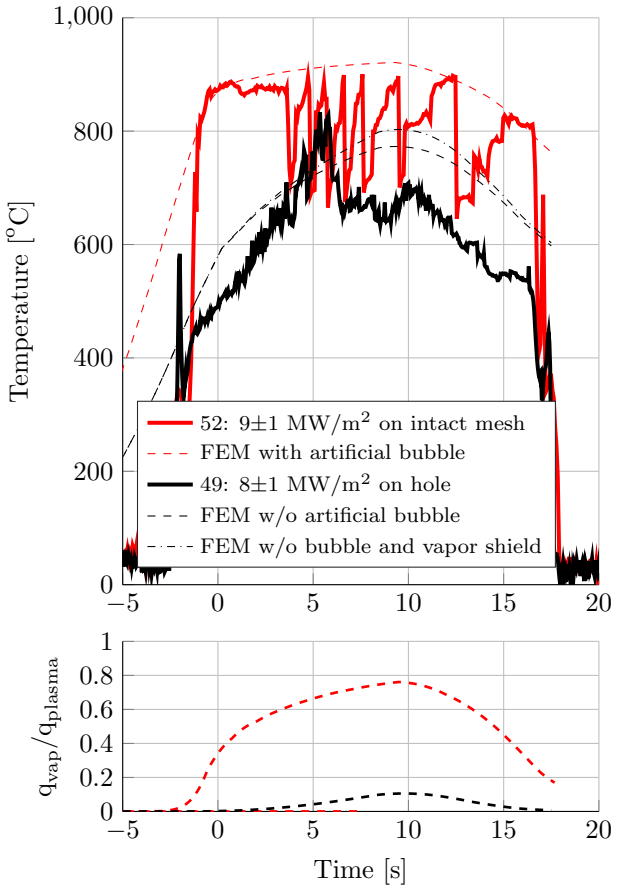

Figure 16. Comparison of the IR-cam measurements on LL to FEM modeling with (black) and without (red) a hole in the mesh. As shown in fig. 15 an artificial bubble must be introduced to match the quick temperature increase in shot 52. The power fraction dissipated by vapor shielding is shown in the bottom pane, evaluated in the exact center of the PFS. vapor shielding appears to be very relevant for shot 52, but does not play a significant role in shot 49.

as pure lithium, and a cylindrical cavity with diameter of 3 mm and height 0.5 mm was inserted 0.25 mm below the surface, see figure 15. The dimensions of this artificial bubble were chosen to best match the experimental results. Results of the FEM modeling are shown in figure 16.

Simulations were also performed to determine the effect of adding only the 0.5 mm lithium layer to the model, and the effect of the bubble size. Adding the Li layer only has a small effect, compared to the model without the layer and bubble. The temperature evolves the same as the black dashed curve, except it lies about 50 °C higher (after 0 s). Hence, the bubble is mainly responsible for the difference between the black and red dashed curves in figure 16. Increasing the bubble diameter from 3 mm to 6 mm results in an increase of the temperature plateau by about 20 to 40 °C. Also vapor shielding becomes relevant about 4 seconds earlier.

The model seems to reconstruct the evolution of the central surface temperature fairly well. The bottom pane of figure 16 shows the fraction of power dissipated via vapor shielding in the exact center of the target model. This indicates that indeed a significant fraction of power must be dissipated via vapor shielding to achieve the temperature plateau in shot 52. Interestingly this is not the case for shot 49. Here, the increased heat conduction due to the lithium is mainly responsible for the temperature reduction. This is also illustrated by the dash-dotted curve, which is still a reasonable match, despite completely neglecting vapor shielding.

To match the experimental results, the redeposition coefficient R needed to be set to 0.9. This seems to be contradicting literature. In [34] and [35] the redeposition of tin and lithium respectively has been investigated and R is found to be >0.999 in both cases. A possible explanation for this discrepancy could be that both these works experiments are conducted in Magnum-PSI where the redeposited species was at an impurity level density several orders of magnitude below the electron density. Furthermore, the samples used in these studies had diameters not exceeding the beam diameter. In this work the target surface width was more than twice the FWHM of the beam, and

lithium density was estimated to be comparable to the plasma density as we are in a vapor shielding regime (though not measured).

Another explanation could be that the model from [7] contains a wrong assumption. It is assumed that only non-redeposited particles dissipate energy. Redeposited particles do dissipate a small amount of energy, namely via radiation. This could form a significant contribution, especially given the high redeposition coefficient. Redeposited particles would dissipate a small amount of energy many times, before being eventually lost. Thus, the effective value of ϵ_{cool} is increased. Given the uncertainty in ϵ_{cool}, it is not possible to determine R accurately.

Any changes to R or ϵ_{cool} will however not impact the vapor shielded power fraction in figure 16, as still the same amount of power must be shielded to obtain the correct temperatures. The amount of lithium needed, though, will reduce. Nevertheless, this will not significantly impact the modeled temperature due to the strong dependence of the evaporation rate on the lithium surface temperature.

Lastly, it was found impossible to accurately estimate the lifetime of the target. This was caused by the following issues: First, it is only possible to roughly estimate the central surface temperature evolution. Second, the uncertainty in R (discussed above) is problematic. Namely, whether R=0.9 or R>0.999 makes a factor 100 difference in the amount of Li lost from the surface under the beam. Third, the degree to which the targets are filled is unknown, especially because some leaking occurs during the experiments. Fourth, due to depletion of the reservoir and wicks, the thermal behavior of the target changed. This must be accounted for in the model. Fifth, on long enough timescales it becomes important to correctly model the thermal connection to the heat sink (i.e. the cooled target holder). This was not the case for the 10 s exposures, but it was the case during the 70 s exposure in shot 77. In this work, sufficient data is not available to check if this thermal connection has been modeled correctly. However, a best and worst case estimate indicate that between 0.1 and 0.6 grams of lithium must have evaporated from outer regions during shot 77 alone. Concluding, ballpark estimates of the lifetime can be made, but not sufficiently accurate to compare the experimental observations. In more controlled environments however, this might be possible.

4.4. Future application

A few important lessons have been learned that are relevant for the design of an LLD for DEMO. Firstly, the experimental observations show the presence of the vapor shielding effect. This means Li targets could be extremely robust against high heat loads, as long as sufficient Li is supplied. The prototypes tested here show that supply through a passive capillary flow can already be sufficient. Furthermore, the power handling model from [7] and the theoretical Li supply rate ($2 \cdot 10^{25}$ $\mathrm{m^{-2}s^{-1}}$, [12]) can be combined to find the theoretical maximum tolerable power. This shows that if the mesh had not failed, the target should have been able to handle around 20 $\mathrm{MW/m^2}$ in Magnum-PSI. However, in a tokamak the dissipated energy per lithium particle would likely be higher (> 50 eV), and a maximum of over 100 $\mathrm{MW/m^2}$ might even be realized. Of course, at this point the evaporative flux is perhaps no longer compatible with fusion conditions.

Second, as it is found possible to roughly estimate the temperature response of the lithium targets, now also thermal stresses can be calculated. This is an important capability for the design of future LLDs. It is expected that stresses in LLDs can be significantly lowered compared to solid divertors. Lithium channels create freedom for thermal expansion, without thermally insulating material or creating leading edges. This is exactly the secondary function of the wicking channels in the pre-filled LLD design, as explained in the introduction. Additionally stresses are lowered because the PFS stays much cooler than solid alternatives.

Third, the evaporation of lithium and its compatibility with fusion conditions remains a concern. As suggested from the FEM modeling, even regions not exposed to the plasma can contribute significantly to the lithium evaporation rate. If the LM concentration in the vacuum vessel is to be kept low in future tokamaks, these regions should be avoided.

Regarding the maximum evaporation rate that can be tolerated: this limit can be experimentally investigated using the concept tested here. Both power handling capabilities and lifetime are sufficient for this purpose, as demonstrated and discussed in 4.1. Upcoming additive manufacturing techniques will make production and use of pre-filled LLD targets even more convenient.

5. Conclusion

Prototypes of pre-filled liquid lithium targets were successfully tested. The prototypes could handle a peak power density of up to 9 $\mathrm{MW/m^2}$ for 10 seconds, beyond which a hole was created in the mesh layer on the PFS. Despite the damage, the targets could continue to function. Poor fixation of the mesh to the surface is suspected to be the cause of the failure. The targets had a total lifetime of up to 100 seconds, though this will likely be longer in a tokamak with short pulses. The performance is deemed sufficient for use on tokamak experiments, e.g. to investigate Li

transport. Though, it is recommended to improve the surface texturing, for example by the use of additive manufacturing.

The central surface temperature evolution of the targets was successfully reconstructed via FEM modeling combined with an analytical approximation of vapor shielding [7]. The modeling as well as the experimental results indicated that vapor shielding plays a significant role in the power dissipation. This implies future LLD designs might be extremely robust against high heat loads, as long as sufficient Li is supplied.

Estimates of the locking temperature are mainly determined by the strong dependence of the evaporation rate on the lithium surface temperature, and are relatively insensitive to other parameters. Both the capability to predict the temperature response, as well as thermal stresses are extremely relevant for design of LLDs for DEMO. Though, accurate prediction of the lifetime was impossible for the prototypes tested here, due to a poorly controlled thermal connection, filling ratio, and insufficient knowledge about the redeposition. The FEM modeling of extreme cases does indicate evaporation from areas not exposed to the plasma might have been a significant loss channel of lithium, due to the lack of redeposition. Areas such as this should be avoided in future designs.

Suggestions for future work

In the near future, it is recommended to carry out tests with transient loading conditions to investigate the impact of ELMs or disruptions. This is possible on Magnum-PSI, and also provides an opportunity to more thoroughly check the predictive capability of the model from [7].

Furthermore, to prevent damage to the mesh layer it is recommended that either the fixation to the substrate is improved, or another suitable texturing is used. This will make the target more robust, and also exclude movement of the mesh as a cause of the oscillatory behavior. An interesting option would be to 3D-print the texturing, or even to print the entire target. Additive manufacturing of tungsten is already commercially available [36, 37].

6. Acknowledgement

This work has been carried out within the framework of the EUROfusion Consortium and has received funding from the Euratom research and training programme 2014-2018 under grant agreement No. 633053. The views and opinions expressed herein do not necessarily reflect those of the European Commission.

Also this work is supported by DIFFER, which is part of the Netherlands Organization for Scientific Research (NWO) and a partner in the Trilateral Euregio Cluster, TEC.

References

[1] J W Coenen, G De Temmerman, G Federici, V Philipps, G Sergienko, G Strohmayer, A Terra, B Unterberg, T Wegener, and D C M Van den Bekerom. Liquid metals as alternative solution for the power exhaust of future fusion devices: status and perspective. *Physica Scripta*, T159(T159):014037, apr 2014.

[2] D.N. Ruzic, W. Xu, D. Andruczyk, M.A. Jaworski, Kaita R. et Al, Xu W. Jaworski M.A., Gray T.K., Antonelli M., Kim J.J., Lau C.Y., Lee M.B., Neumann M.J., Ruzic D.N., Shercliff J.A., Morley N.B. Jaworski M.A., Ruzic D.N., Jaworski M.A., Ruzic D.N. Surla V., Tung M., Xu W., Andruczyk D., Neumann M., Mansfield D., Majeski R. Jaworski M.A., Gerhardt S.P., Morley N.B., Abrams T., Kaita R., Kallman J., Kugel H., and Ruzic D.N. Lithiummetal infused trenches (LiMIT) for heat removal in fusion devices. *Nuclear Fusion*, 51(10):102002, oct 2011.

[3] S. V. Mirnov, E. A. Azizov, V. A. Evtikhin, V. B. Lazarev, I. E. Lyublinski, A. V. Vertkov, and D. Yu Prokhorov. Experiments with lithium limiter on T-11M tokamak and applications of the lithium capillary-pore system in future fusion reactor devices. *Plasma Physics and Controlled Fusion*, 48(6):821–837, 2006.

[4] L.G. Golubchikov, V.A. Evtikhin, I.E. Lyublinski, V.I. Pistunovich, I.N. Potapov, and A.N. Chumanov. Development of a liquid-metal fusion reactor divertor with a capillary-pore system. *Journal of Nuclear Materials*, 233-237:667–672, oct 1996.

[5] M A Jaworski, A Khodak, and R Kaita. Liquid-metal plasma-facing component research on the National Spherical Torus Experiment. *Plasma Physics and Controlled Fusion*, 55(12):124040, 2013.

[6] G. G. van Eden, T. W. Morgan, D. U. B. Aussems, M. A. van den Berg, K. Bystrov, and M. C. M. van de Sanden. Self-Regulated Plasma Heat Flux Mitigation Due to Liquid Sn Vapor Shielding. *Physical Review Letters*, 116(13):135002, apr 2016.

[7] P. Rindt, T.W. Morgan, M.A. Jaworski, and N.J. Lopes Cardozo. Power handling limit of liquid lithium divertor targets. *Nuclear Fusion*, 58(10):104002, oct 2018.

[8] C.N. Taylor, K.E. Luitjohan, B. Heim, L. Kollar, J.P. Allain, C.H. Skinner, H.W. Kugel, R. Kaita, A.L. Roquemore, and R. Maingi. Surface chemistry analysis of lithium conditioned NSTX graphite tiles correlated to plasma performance. *Fusion Engineering and Design*, 88(12):3157–3164, dec 2013.

[9] G. Mazzitelli, M.L. Apicella, D. Frigione, G. Maddaluno, M. Marinucci, C. Mazzotta, V. Pericoli Ridolfini, M. Romanelli, G. Szepesi, O. Tudisco, and FTU Team. FTU results with a liquid lithium limiter. *Nuclear Fusion*, 51(7):073006, jul 2011.

[10] J Ren, J S Hu, G Z Zuo, Z Sun, J G Li, D N Ruzic, and L E Zakharov. First results of flowing liquid lithium limiter in HT-7. *Physica Scripta*, 2014(T159):14033, 2014.

[11] B.I. Khripunov, V.B. Petrov, V.V. Shapkin, N.V. Antonov, A.S. Pleshakov, A.S. Rupyshev, D.Yu. Prokhorov, V.A. Evtikhin, I.E. Lyublinsky, and V.V. Vertkov. Lithium surface operating under steady-state power load. *Fusion Engineering and Design*, 65(3):449–454, apr 2003.

[12] P. Rindt, N.J. Lopes Cardozo, J.A.W. van Dommelen, R. Kaita, and M.A. Jaworski. Conceptual design of a pre-loaded liquid lithium divertor target for NSTX-U. *Fusion Engineering and Design*, 112, 2016.

[13] S V Mirnov, E A Azizov, V A Evtikhin, V B Lazarev,

I E Lyublinski, A V Vertkov, and D Yu Prokhorov. Experiments with lithium limiter on T-11M tokamak and applications of the lithium capillary-pore system in future fusion reactor devices. *Plasma Physics and Controlled Fusion*, 48(6):821, 2006.

[14] A. Sestero. Protection of walls from hard disruptions in large tokamaks. *Nuclear Fusion*, 17(1):115–123, feb 1977.

[15] D. I. Skovorodin, A. A. Pshenov, A. S. Arakcheev, E. A. Eksaeva, E. D. Marenkov, and S. I. Krasheninnikov. Vapor shielding models and the energy absorbed by divertor targets during transient events. *Physics of Plasmas*, 23(2):022501, feb 2016.

[16] G G van Eden, V Kvon, M C M van de Sanden, and T W Morgan. Oscillatory vapour shielding of liquid metal walls in nuclear fusion devices. *Nature communications*, 8(1):192, 2017.

[17] R.J. Goldston, A. Hakim, G.W. Hammett, M.A. Jaworski, and J. Schwartz. Recent advances towards a lithium vapor box divertor. *Nuclear Materials and Energy*, 12:1118–1121, aug 2017.

[18] H.J.N. van Eck, T. Abrams, M.A. van den Berg, S. Brons, G.G. van Eden, M.A. Jaworski, R. Kaita, H.J. van der Meiden, T.W. Morgan, M.J. van de Pol, J. Scholten, P.H.M. Smeets, G. De Temmerman, P.C. de Vries, and P.A. Zeijlmans van Emmichoven. Operational characteristics of the high flux plasma generator Magnum-PSI. *Fusion Engineering and Design*, 89(9):2150–2154, 2014.

[19] G De Temmerman, M A van den Berg, J Scholten, A Lof, H J van der Meiden, H J N van Eck, T W Morgan, T M de Kruijf, P A Zeijlmans van Emmichoven, and J J Zielinski. High heat flux capabilities of the Magnum-PSI linear plasma device. *Fusion Engineering and Design*, 88(68):483–487, 2013.

[20] H.J.N. van Eck, W.R. Koppers, G.J. van Rooij, W.J. Goedheer, B. de Groot, P. Smeets, J. Scholten, M. van de Pol, S. Brons, R. Koch, B. Schweer, U. Samm, V. Philipps, R.A.H. Engeln, D.C. Schram, N.J. Lopes Cardozo, and A.W. Kleyn. Pre-design of Magnum-PSI: A new plasmawall interaction experiment. *Fusion Engineering and Design*, 82(15):1878–1883, 2007.

[21] J. Rapp, W.R. Koppers, H.J.N. van Eck, G.J. van Rooij, W.J. Goedheer, B. de Groot, R. Al, M.F. Graswinckel, M.A. van den Berg, O. Kruyt, P. Smeets, H.J. van der Meiden, W. Vijvers, J. Scholten, M. van de Pol, S. Brons, W. Melissen, T. van der Grift, R. Koch, B. Schweer, U. Samm, V. Philipps, R.A.H. Engeln, D.C. Schram, N.J. Lopes Cardozo, and A.W. Kleyn. Construction of the plasma-wall experiment Magnum-PSI. *Fusion Engineering and Design*, 85(7-9):1455–1459, dec 2010.

[22] Dutch Institute For Fundament Energy Research. www.differ.nl/research/fusion-facilities-and-instrumentation/magnum-psi/application-form.

[23] M.J Baldwin, R.P Doerner, S.C Luckhardt, and R.W Conn. Deuterium retention in liquid lithium. *Nuclear Fusion*, 42(11):1318–1323, nov 2002.

[24] S K Erents, G M McCracken, and P Goldsmith. Trapping of keV deuterons in lithium. *Journal of Physics D: Applied Physics*, 4(5):305, may 1971.

[25] P. Rindt. 4TU - Dataset: Power handling and vapor shielding of pre-filled lithium divertor targets.

[26] C. Cagran, G. Pottlacher, M. Rink, and W. Bauer. Spectral Emissivities and Emissivity X-Points of Pure Molybdenum and Tungsten. *International Journal of Thermophysics*, 26(4):1001–1015, jul 2005.

[27] M. Rosenberg, R.D. Smirnov, and A. Yu. Pigarov. On thermal radiation from fusion related metals. *Fusion Engineering and Design*, 84(1):38–42, jan 2009.

[28] Plansee. www.plansee.com/en/materials/molybdenum.html.

[29] Grafoil Engineering Design Manual, 2002.

[30] V.G. Belan, V.F. Levashov, V.S. Maynashev, A.D. Muzichenko, and V.L. Podkovirov. Features of dynamics and structure of the shielding layer at the interaction of plasma flow with target. *Journal of Nuclear Materials*, 233-237:763–766, oct 1996.

[31] V I Tereshin, A N Bandura, O V Byrka, V V Chebotarev, I E Garkusha, I Landman, V A Makhlaj, I M Neklyudov, D G Solyakov, and A V Tsarenko. Application of powerful quasi-steady-state plasma accelerators for simulation of ITER transient heat loads on divertor surfaces. *Plasma Physics and Controlled Fusion*, 49(5A):A231–A239, may 2007.

[32] V.A. Evtikhin, I.E. Lyublinski, A.V. Vertkov, V.G. Belan, I.K. Konkashbaev, and L.B. Nikandrov. Calculation and experimental investigation of fusion reactor divertor plate and first wall protection by capillary-pore systems with lithium. *Journal of Nuclear Materials*, 271-272:396–400, may 1999.

[33] R.C. Wieggers, D.P. Coster, P.W.C. Groen, H.J. de Blank, and W.J. Goedheer. B2.5-Eunomia simulations of Pilot-PSI plasmas. *Journal of Nuclear Materials*, 438:S643–S646, jul 2013.

[34] V. Kvon, R. Al, K. Bystrov, F.J.J. Peeters, M.C.M. van de Sanden, and T.W. Morgan. Tin re-deposition and erosion measured by cavity-ring-down-spectroscopy under a high flux plasma beam. *Nuclear Fusion*, 57(8):086040, aug 2017.

[35] T Abrams. *Erosion and Re-Deposition of Lithium and Boron Coatings Under High-Flux Plasma Bombardment*. Phd. thesis, Princeton University, 2015.

[36] DUNLEE — 3D Metal Printing. www.dunlee.com/a-w/3d-metal-printing/our-offer.html.

[37] Wolfmet 3D Printed Tungsten. www.wolfmet.com/applications/slm/.